Copper Supported on Ceria Mesocellular Foam Silica as an Effective Catalyst for Reductive Condensation of Acetone to Methyl Isobutyl Ketone

Grzelak, Kalina; Trejda, Maciej; Riisager, Anders

Published in:
ChemSusChem

Link to article, DOI:
10.1002/cssc.202102012

Publication date:
2022

Document Version
Peer reviewed version

WILEY-VCH

FULL PAPER

Copper-ceria mesocellular foam silica as effective catalyst for the reductive condensation of acetone to methyl isobutyl ketone

Kalina Grzelak[a], Maciej Trejda*[a] and Anders Riisager*[b]

[a] K. Grzelak, Dr. M. Trejda,
Department of Heterogeneous Catalysis
Faculty of Chemistry, Adam Mickiewicz University, Poznań
ul. Uniwersytetu Poznańskiego 8, 61-614 Poznań, Poland
tmaciej@amu.edu.pl

[b] Prof. A. Riisager
Centre for Catalysis and Sustainable Chemistry
Department of Chemistry, Technical University of Denmark
Kemitorvet, Building 207, 2800 Kgs. Lyngby, Denmark
ar@kemi.dtu.dk

Supporting information for this article is given via a link at the end of the document.

Abstract: Copper-containing materials based on Ce- and Ca-Nb-mesocellular foam (MCF) silica supports were prepared, characterized and applied as catalysts for gas-phase, reductive condensation of acetone to produce methyl isobutyl ketone (MIBK). The properties of the materials as well as the interaction of metal species and their role in the catalytic process were examined by nitrogen physisorption, XRD, XPS, CO_2-TPD, H_2-TPR and chemisorption of NO and pyridine combined with FTIR. A synergetic interaction of Cu^{2+}, Cu^0 and CeO_2 species incorporated in the MCF support allowed obtaining a Cu/Ce-MCF catalyst yielding 34% of acetone conversion with over 90% MIBK selectivity at 250 ˚C, and this high catalyst selectivity was maintained during operation for 24 h despite the catalyst activity decline. The obtained catalytic performance is superior to that of Cu/HAP and similar Pd-containing catalyst previously reported in literature.

Introduction

Many industrial processes apply liquid alkaline media for catalytic condensation reactions, e.g. aldol condensations.[1] However, solid basic catalysts have become attractive alternatives because such materials are non-corrosive and easily separated from the reaction mixture. The industrial production of methyl isobutyl ketone (MIBK) from acetone is a multistep process as shown in Scheme 1. In the first two steps, acetone undergoes condensation and dehydration to mesityl oxide under alkaline (or acidic) conditions, whereas the latter is reduced with hydrogen to MIBK over metallic sites in a final step. Many different supports have been applied as catalysts for the two first steps in the MIBK production, while preferable metals chosen for the hydrogenation step have been Pd[2-14] and other noble metals like Pt[9,15–17] and Rh.[18] Noble metals are known to be efficient in hydrogenation reactions, however, their high cost has stimulated the search for cheaper alternatives like Ni[9,19,20] and Cu.[9,21–24]

For gas-phase MIBK production, Waters et al.[9] have compared various metal/carbon catalysts for the hydrogenation step and ordered the catalytic performance of the metals in the sequence Pt > Pd > Ni > Cu. The Cu catalyst produced most coke of the examined catalysts and only high loading of Ni yielded similar catalytic performance as the most active Pt catalyst with low metal loading. Recently, Cu has been frequently chosen as a metal for carbon-oxygen hydrogenation. Although it is documented to be effective in hydrogenation of such compounds as dimethyl oxalate, methyl acetate, furfural or CO_2 to alcohols, its application is still challenging due to the catalyst instability and quick deactivation.[25] Strategies to extend Cu catalyst lifetime include doping with another metal and loading on a high-surface area material to prevent particle agglomeration. Dong et al. reported that In doping to Cu/SBA-15 enhanced its activity in the selective hydrogenation of acetic acid to ethanol.[26] In another work,[27] Chen et al. presented a catalytic system of Cu and La loaded on SBA-15 which was highly selective and active for CO_2 hydrogenation to methanol, which was not the case for the monometallic Cu counterpart. Moreover, the catalyst with optimized La loading was stable for four times as long time on stream as the Cu/SBA-15 catalyst. Additionally, Torres et al.[22] used mixed copper oxide catalysts based on Mg, Al and Ce for obtaining MIBK *via* catalytic transfer-hydrogenation with 2-propanol. The MIBK formation rates were found to be highest over CuCeOx and CuMgAlOx, and it was established that at least 2 wt.% Cu loading was required for efficient catalytic performance. The positive effect of coexistence of Cu and ceria on catalytic performance has been well recognized,[28] especially for redox reactions where electron interaction between the components has been reported to improve catalytic activity.[29–31] For example, when ceria and silica were compared as supports for CO and CO_2 hydrogenation to methanol,[32] an enhanced product selectivity for Cu/CeO_2 compared to Cu/SiO_2 was explained by a higher dispersion of Cu over ceria caused by metal-support interactions. Recently, we reported high stability and selectivity, but moderate activity, of Pd/Ce-MCF (mesocellular foam) catalysts for the gas-phase reductive condensation of acetone to MIBK.[33] In this work we have extended the study by substituting the noble metal Pd with the cheaper metal Cu in Ce-MCF catalysts to explore the possible superior catalytic properties with the combination of Cu and ceria. The new Cu/Ce-MCF catalysts were characterized by multiple techniques to corroborate synergetic properties between Cu and ceria, and the catalytic performance compared to an analogous Cu/Ca-Nb-MCF catalyst.

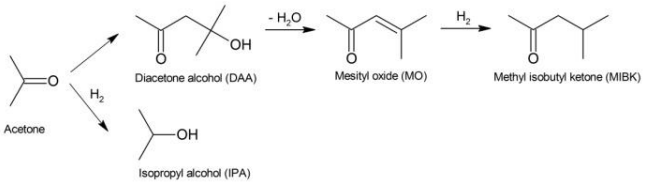

Scheme 1. Reaction pathways for methyl isobutyl ketone (MIBK) and isopropyl alcohol (IPA) formation from acetone.

Results and Discussion

Textural and structural properties of catalysts

The textural properties of mesoporous Ca-Nb-MCF and Ce-MCF supports as well as mesoporous aluminophosphate oxynitridate (MAPN), aluminophosphate (MAP) and hydroxyapatite (HAP) were determined by nitrogen physisorption in our previous work.[33] After impregnation of the mesoporous supports with copper species, all of the resulting materials Cu/Ca-Nb-MCF, Cu/Ce-MCF and Cu/MAPN maintained their mesoporous character with typical nitrogen isotherms of type IVa with H1 hysteresis loops (Figure S1). The modification with Cu led to some decrease in surface area and pore volume for Cu/Ca-Nb-MCF and Cu/Ce-MCF compared to the pristine MCF supports, but they remained still relatively high at 206 and 464 $m^2 g^{-1}$ and 0.91 and 1.43 $cm^3 g^{-1}$, respectively (Table 1). Notably, the surface area of Cu/MAPN was about 2-4.5 times lower than that of the Cu-containing MCF materials, however, these changes resulted mainly from the oxynitridation process of the pristine MAP support and to a minor extent from the introduction of the copper species (Table 1).

Table 1. Textural parameters of the supports and catalysts.

Material	BET area [$m^2 g^{-1}$]	Pore diameter [nm]		Pore vol. [$cm^3 g^{-1}$]
		Adsorption	Desorption	
Ca-Nb-MCF [a], [33]	276	22.9	11.1	1.03
Cu/Ca-Nb-MCF [a]	206	22.4	12.8	0.91
Ce-MCF [a], [33]	487	22.4	15.6	1.58
Cu/Ce-MCF [a]	464	23.2	14.1	1.43
HAP [b], [33]	61	30.6	-	0.38
Cu/HAP [b]	52	47.8	-	0.37
MAP [c], [33]	275	11.8	-	0.46
MAPN [c], [33]	125	11.8	-	0.26
Cu/MAPN [c]	107	10.1	-	0.22

[a] Pore volume and cell diameter were determined from adsorption branches of N_2 isotherms. Window diameter determined from desorption branches of N_2 isotherms by BdB-Fass method. [b] Pore volume and diameter determined from adsorption branches of N_2 isotherms by BJH method with Kruk-Jaroniec-Sayaroi correction. [c] Pore volume and diameter determined from adsorption branches of N_2 isotherms by DFT.

The HAP support had the smallest surface area (61 $m^2 g^{-1}$) of the applied supports and after Cu impregnation the resulting material Cu/HAP had even lower surface area, but practically unchanged pore volume (Table 1) and unchanged crystalline HAP structure as shown by XRD (Figure S2). A more detailed examination of the nitrogen isotherms of Cu/HAP (Figure S1) revealed a hysteresis loop at high relative pressure p/p_o indicating presence of large mesopores or macropores probably originating from intraparticle voids. Combined this suggests that the copper species were located mainly on the surface of the support and not inside the pores of the Cu/HAP material.

State of metal species in catalysts

The XRD pattern of Cu/Ce-MCF (Figure 1) exhibited reflections at 35.5 and 38.7° assignable to CuO crystallites[31,34,35] with an average size of 7 nm calculated by the Scherrer equation. Likewise, for Cu/HAP the presence of CuO was evident by the reflection at 38.7° (Figure S2), whereas other reflections was probably overlapped with reflections from the HAP support. In contrast, no reflections from crystalline copper species were found in the XRD diffractograms of Cu/Ca-Nb-MCF (Figure 1) and Cu/MAPN (Figure S2), suggesting that the copper species in these samples were either very small and well dispersed or amorphous.

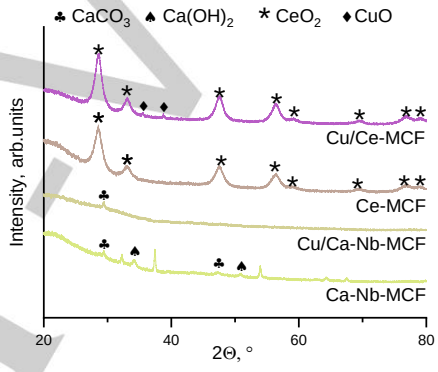

Figure 1. XRD diffractograms of Ce-MCF and Ca-Nb-MCF supports and corresponding Cu/Ce-MCF and Cu/Ca-Nb-MCF catalysts.

The XP spectrum of Cu/Ca-Nb-MCF (Figure 2) revealed an intense Cu $2p_{3/2}$ signal typical of Cu^{2+} at 935.0 eV with characteristic satellites at ca. 943.5 eV. However, the binding energy (BE) was much higher than reported for CuO.[36] Copper species can interact with silica supports to form Cu^{2+}-O-Si groupings,[37] and such strong metal-support interaction results in charge-transfer from the metal ion to the silica support and higher BE, as previously reported for Nb species.[38,39] The presence of Cu^{2+}-O-Si on the catalyst surface instead of CuO species is in accordance with the XRD measurements, where none of the latter species were found. After pretreatment with H_2 at 350 °C the satellites at ca. 943.5 eV disappeared and Cu $2p_{3/2}$ signal was shifted to 933.5 eV indicating the reduction of copper species (Figure S3). In the XP spectrum of the material in the Nb 3d regions (Figure S4) bands assigned to Nb $3d_{3/2}$ and Nb $3d_{5/2}$ at 210.9 and 208.1 eV, respectively, were consistent with presence of Nb(V). Notably, also here the observed BE was also much higher than the value typical of niobium(V) oxide further corroborating strong metal-support interactions.

The XP spectrum of Cu/Ce-MCF in the Cu 2p region differed from that of Cu/Ca-Nb-MCF (Figure 2) and showed a symmetric Cu $2p_{3/2}$ signal at 932.9 eV, characteristic of Cu^+ or Cu^0,[40,41] and no Cu^{2+} satellites. After pretreatment with H_2 at 350 °C, the Cu $2p_{3/2}$ signal was almost unchanged except a slight shift to lower energy (932.8 eV) (Figure S3). The lack of satellites indicated that Cu was partially reduced, however, the XRD pattern of Cu/Ce-MCF also

clearly confirmed reflections from CuO species (Figure 1). To identify the reduced form of Cu, NO adsorption combined with FTIR spectroscopy was applied as NO adsorbs on copper cations forming specific complexes. After NO adsorption, the spectrum of Cu/Ce-MCF (Figure S5) showed two characteristic bands of Cu^{2+} interacting with NO at 1621 cm^{-1}, assigned to $Cu^{2+}(O^{-}NO)(NO)$, and 1879 cm^{-1} assigned to $Cu^{2+}NO$,[42,43] but no band at ca. 1810 cm^{-1} typical of Cu^{+} interacting with NO. This indicated that the reduced species formed (and measured by XPS) were Cu^{0}. Oppositely, were Cu^{2+} species only detected in the FTIR spectrum of Cu/Ca-Nb-MCF after NO adsorption (Figure S5).

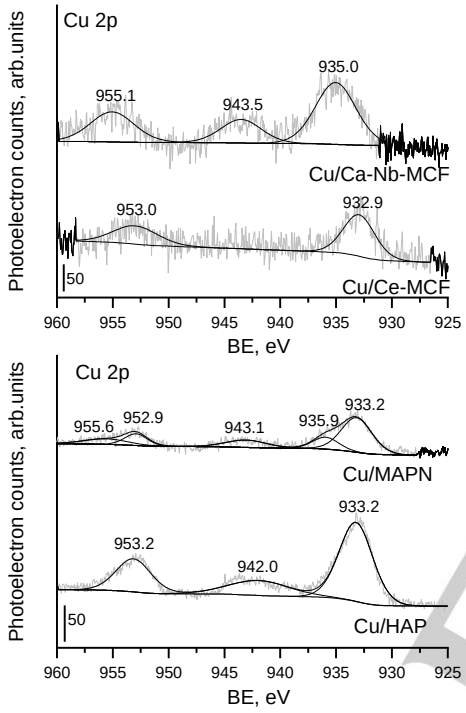

Figure 2. XP spectra in the Cu 2p region of Cu/Ca-Nb-MCF and Cu/Ce-MCF catalysts (top), and Cu/MAPN and Cu//HAP catalysts (bottom).

Cu/Ce-MCF was also examined by XPS in the Ce 3d region and revealed predominantly Ce^{4+} from CeO_2 oxide (Figure S4), in agreement with the XRD pattern (Figure 1). However, the spectrum could be deconvoluted into three pairs of signals at 883.0 and 901.3 eV, 889.8 and 907.7 eV, 898.5 and 916.9 eV. assigned to Ce^{4+} and one pair of signals at 887.2 and 904.7 eV assigned to Ce^{3+} with calculated $Ce^{3+}/(Ce^{3+}+Ce^{4+})$ ratio 0.044.[44–46] Ce^{3+} and Ce^{4+} species exhibit redox properties and under oxidizing conditions ceria can interact with other transition metals inducing electron-transfer towards that metal,[28] resulting in local oxidization of ceria and metal reduction. This phenomenon may explain the reduction of copper species observed for the Cu/Ce-MCF material by XPS. However, it is very likely that some Ce^{3+} and oxygen vacancies remained after the reduction due to the higher concentration of cerium species compared to copper species.

The XP spectra of Cu/Ce-MCF and Cu/Ca-Nb/MCF in the O 1s region (Figure S6) were also recorded and analyzed. Here two bands were found and assigned to oxygen in the silica lattice at ca. 533 eV (more intense band) and to oxygen in ceria or copper oxide at ca. 531.2 eV, respectively.[47] The later band has been also assigned in literature to adsorbed CO_2. [48,49] The intensity of band at ca. 531.2 eV decreased after hydrogen pretreatment of Cu/Ce-MCF confirming the effective reduction of the oxide species. Oppositely, for Cu/Ca-Nb-MCF the relative band intensity at ca. 531.2 eV associated to calcium-, niobium- and copper oxides in Cu/Ca-Nb-MCF was less effected by the hydrogen treatment (Figure S4). Moreover, it was also noticed that Ca^{2+} species were detected (band at 347.9 eV) after the treatment with hydrogen, while Nb^{5+} species were not reduced (Figure S4).

XPS analyses were also performed with the reference materials Cu/MAPN and Cu/HAP (Figure 2). The Cu 2p region of the former was deconvoluted into two signals at 933.2 eV and 935.9 eV assigned to Cu^{+} (or Cu^{0}) and Cu^{2+}, respectively, with well-distinguished satellites in the region of 940-945 eV indicative of CuO. However, the BE of Cu^{2+} was like for Cu/Ca-Nb-MCF shifted to a higher value than typical of CuO, and CuO species were not detected by XRD (see above). Accordingly, it may be speculated that other surface species formed maybe by interaction with aluminum, i.e. Cu^{2+}-O-Al. In contrast, the state of the copper species in Cu/HAP were similar to that of Cu/Ce-MCF revealing a rather symmetric band at 932.7 eV assignable to Cu_2O or Cu^{0}. The intense satellites suggested presence of CuO, which was also confirmed by XRD analysis (Figure S2). For both reference materials the pretreatment with H_2 at 350 ˚C resulted only in a slight shift of the Cu $2p_{3/2}$ signal to a 0.2-0.3 eV lower BE, but only for Cu/MAPN were the satellites in the region of 940-945 eV still visible (Figure S3).

Basicity and acidity of catalysts

The conversion of acetone to MIBK consist of three catalytic steps involving i) condensation of acetone to diacetone alcohol (DAA) over basic sites, ii) dehydration of DAA to mesityl oxide (MO) on acidic sites and iii) hydrogenation of MO to MIBK on metallic sites (Scheme 1), thus making catalyst basicity and acidity important for the catalytic performance.

Table 2. TPD-CO_2 data of the catalysts.

Catalyst	Desorbed CO_2 [mmol g^{-1}_{cat} $\cdot 10^{-3}$]
Cu/Ca-Nb-MCF	2.33
Pd/Ca-Nb-MCF [33]	3.36
Cu/Ce-MCF	2.41
Pd/Ce-MCF [33]	2.02
Cu/HAP	3.39
Pd/HAP [33]	3.79
Cu/MAPN	3.34
Pd/MAPN [33]	2.90

CO_2-TPD was performed on the Cu-modified materials to examine their basicity (Figure S7) and the results are compiled in Table 2. The Cu-modified MCF's possessed almost the same number of basicity with a desorption maximum at 111 °C for Cu/Ca-Nb-MCF and 93 °C for Cu/Ce-MCF. An additional desorption peak of the latter catalyst at 269 °C most probably originated from the presence of cerium species as the related signal was also reported for Ce-MCF.[33] The Cu/Ca-Nb-MCF and Cu/HAP catalysts were less basic than their Pd-counterparts,

whereas Cu/Ce-MCF and Cu/MAPN were more basic than the analogous Pd-catalysts. Such variations may originate from differences in the interaction between metals on the catalyst surfaces.

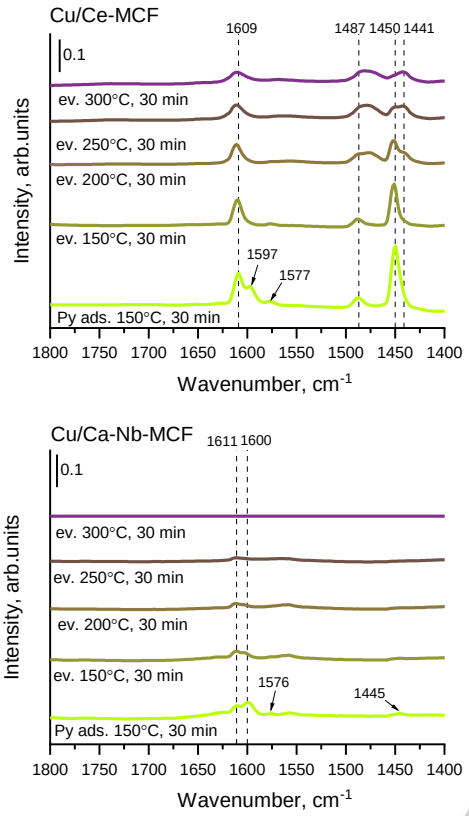

Figure 3. FTIR spectra of Cu/Ce-MCF (top) and Cu/Ca-Nb-MCF (bottom) after pyridine adsorption at 150 ˚C and consecutive evacuations at 150, 200, 250 and 300 ˚C, respectively.

Acidity of the Cu-MCF catalysts were evaluated by FTIR after pyridine adsorption and the results are shown in Figure 3. After pyridine adsorption and outgassing for 10 min, physisorbed pyridine remained on the catalysts as indicated by the bands at 1577 and 1597 cm^{-1} assigned to hydrogen-bonded pyridine. However, these bands disappeared after outgassing at 150 °C for 30 min leaving only bands at ca. 1450 and 1610 cm^{-1} of pyridine bound to Lewis acid sites (LAS) on the catalyst.[50] In the Cu/Ce-MCF spectrum both bands were clearly visible confirming the presence of LAS, while the band at similar position (1445 cm^{-1}) for Cu/Ca-Nb-MCF was much less intense indicating a significantly lower LAS density. Moreover, the band almost disappeared after outgassing at 150 °C for 30 min revealing relative weak LAS in the Cu/Ca-Nb-MCF catalyst, while stronger LAS were present in the Cu/Ce-MCF catalyst where the band remained even after treatment at 300 °C. Notably, the band at 1450 cm^{-1} was apparently split into two bands for Cu/Ce-MCF after outgassing at 200 °C and above, suggesting the presence of two kinds of LAS. For both catalyst, a lack of signal at ca. 1550 cm^{-1} indicated no presence of Brønsted acid sites (BAS).

Interaction of metal species in catalysts

To evaluate the interaction between Cu and Ce in more detail, H_2-TPR measurements were performed up to 400 °C with Cu/MCF, Ce-MCF and Cu/Ce-MCF (Figure 4), where the latter was found by XPS (see above) to contain Cu^0 and Cu^{2+}. The H_2-TPR profile of Cu/Ce-MCF revealed four reduction peaks at 169, 192 (most intense), 229 and 261 °C, respectively, whereas Cu/MCF only had a single reduction peak at 233 °C and Ce-MCF showed no reduction peaks as ceria requires temperatures above 500 °C to be reduced.[51,52]

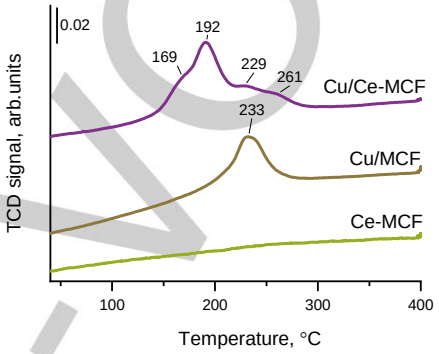

Figure 4. H_2-TPR profiles of Cu/Ce-MCF (top), Cu/MCF (middle) and Ce-MCF (bottom).

It is reported in the literature, that ceria influences the reducibility of copper species giving rise to multiple peaks in H_2-TPR profiles. These peaks are often described as α, β and γ peaks with the low-temperature α peak assigned to finely dispersed copper species,[30,31,35,48,53] intermediate-temperature β peak assigned to larger copper oxide species[31,35] and high-temperature γ peak assigned to bulk copper oxide.[31,34,35,53,54] However, some reports further suggest that the copper species related to the α and β peaks are interacting with oxygen in the ceria,[34,53,54] and an additional high-temperature peak originating from Cu incorporated into the ceria lattice (δ peak) can appear, because such species are more difficult to reduce.[31,53] Zhu et al. also postulated that a high-temperature peak at 279 °C for CuO-CeO_2 corresponded to a mixture of Cu^+ and bulk CuO species.[48] Based on these analyses, the α peak (169 °C) observed for Cu/Ce-MCF represented highly dispersed copper oxide species interacting with ceria surface particle, the intense β peak (192 °C) corresponded to larger copper oxide particles, which were also visible in the XRD pattern, and the γ peak (229 °C) was related to bulk CuO. With respect to the last high-temperature peak (261 °C), the XPS and NO adsorption data of Cu/Ce-MCF (see above) confirmed Cu was partially reduced to Cu^0 and not Cu^+, and the cell parameter of ceria calculated from the XRD of Cu/Ce-MCF (0.538846 nm) was smaller than in Ce-MCF (0.540601 nm) (details on calculation see Supporting Information). Taking into account that the radius of Cu^{2+} is smaller than Ce^{4+} incorporation of Cu into the ceria lattice could cause the observed cell contraction, and the peak was therefore assigned to Cu incorporated into the ceria lattice (i.e. δ peak).

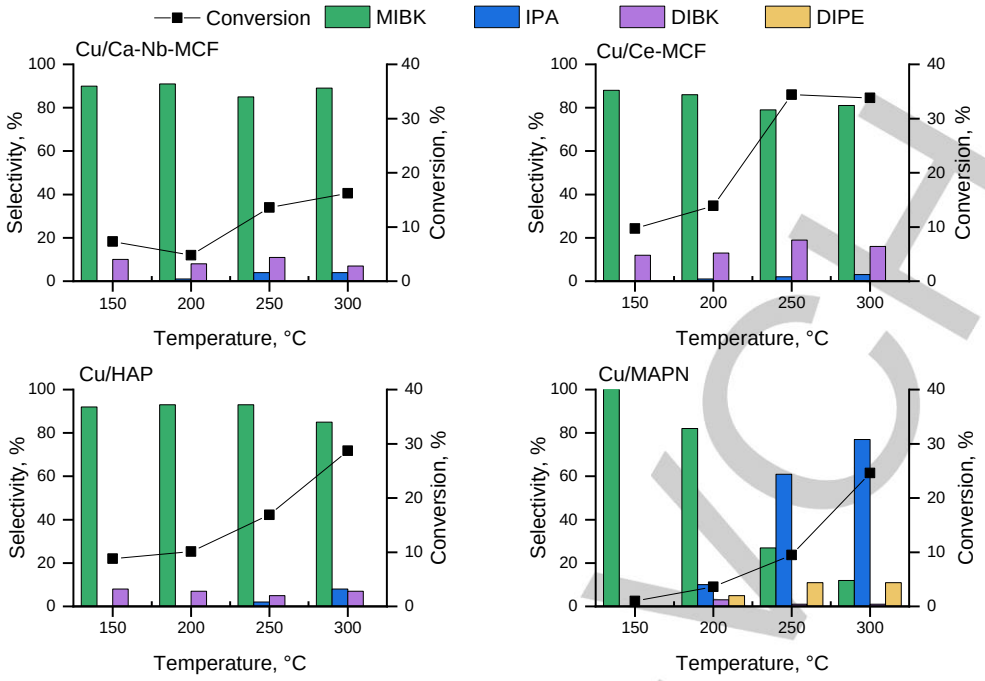

Figure 5. Catalytic performance of Cu/Ca-Nb-MCF, Cu/Ce-MCF, Cu/HAP and Cu/MAPN in the reductive condensation of acetone (MIBK: methyl isobutyl ketone, IPA: isopropyl alcohol, DIBK: diisobutyl ketone, DIPE: diisopropyl ether). Reaction conditions: Acetone (0.05 cm^3 min^{-1}), hydrogen (50 cm^3 min^{-1}), 1 bar.

Catalytic performance

All the Cu-catalysts were applied for the reductive gas-phase condensation of acetone at four temperatures 150, 200, 250, 300 °C and the results are shown in Figure 5. The two Cu-MCF catalysts provided at all temperatures comparable, high selectivity (79-91%) towards MIBK with diisobutyl ketone (DIBK) as a minor byproduct with Cu/Ce-MCF yielding a superior acetone conversion compared to Cu/Ca-Nb-MCF. Importantly, the Cu-MCF catalysts exhibited also better catalytic performance than previously reported for their Pd-based counterparts,[33] particularly the Cu/Ce-MCF catalyst at 250 °C (34% conversion, 79% MIBK selectivity). The Cu/HAP catalyst exhibited also excellent selectivity toward MIBK (85-93%) at 150-300 °C, however, the acetone conversion was significantly lower than for the Cu/Ce-MCF catalyst at all temperatures. Oppositely, Cu/MAPN was only highly selective to MIBK at lower temperatures (i.e. 150 and 200 °C), whereas isopropyl alcohol (IPA) was the major product at higher temperature. Interestingly, this selectivity trend was quite opposite to Pd/MAPN, which was only selective to MIBK at temperature of 300 °C. [33] At higher temperatures, some etherification of IPA to diisopropyl ether (DIPE) was also inevitable for both MAPN-based catalysts due to the acidic character of the support. [33]

To corroborate the influence of Cu on the catalytic performance, the Cu/MCF catalyst without cerium-doping was also applied for the reaction (Figure S8). The catalyst showed very low acetone conversion reaching only 5% at 300 °C, while the MIBK selectivity decreased from 90% at 250 °C to 76% with DIBK as the main byproduct (21% selectivity). This clearly indicated that copper species promoted the condensation towards MIBK. In previous work,[33] an analogous Ce-MCF catalyst was found to provide 12% acetone conversion at 300 °C with insignificant production of MIBK (17% selectivity), clearly implying that a synergistic effect between Cu and Ce improved the activity of the Cu/Ce-MCF catalyst. Moreover, Ca-Nb-MCF and HAP supports were also previously found to give low MIBK yields further indicating the essential contribution of Cu in the process.[33]

Long-term performance of catalysts

Finally, the activity of the two most active catalysts Cu/Ce-MCF and Cu/HAP were evaluated in prolonged reactions at 250 °C for 24 h and the results are presented in Figure 6. The Cu/Ce-MCF catalyst lost within the first 3 h of reaction about 50% of its initial activity, where after the acetone conversion remained constant around 17%. Concurrently, the MIBK selectivity increased steadily from 80% up to ca. 90% during the reaction. The Cu/HAP material had much higher initial acetone conversion (ca. 65%) compared to the Cu/Ce-MCF, but the acetone conversion decreased gradually over time reaching only 12% after 24 h of reaction without stabilizing and the MIBK selectivity fluctuated between 60-90% in the first 17 h before reaching a high constant value of 94%. Hence, both of the catalysts remained highly selectivity towards MIBK but lost significant activity over time, and only the Cu/Ce-MCF catalyst remained stable during the long-term test. A similar loss in activity was not observed for the analogous Pd/Ce-MCF catalyst,[33] however, the catalytic performance of the Cu/Ce-MCF catalyst was higher than over Pd/Ce-MCF despite the initial decrease in activity (Figure S9).

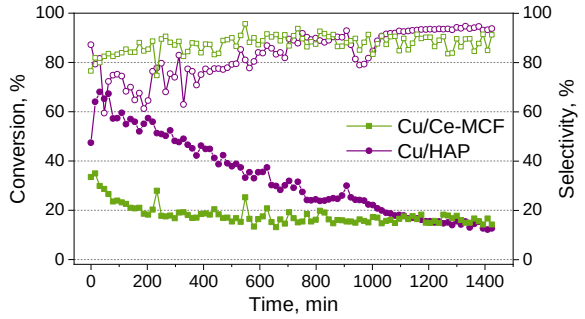

Figure 6. Catalytic performance of Cu/Ce-MCF (green line) and Cu/HAP (purple line) in the reductive condensation of acetone during 24 h time-on-stream (acetone conversion: filled symbols, MIBK selectivity: open symbols, MIBK: methyl isobutyl ketone). Reaction conditions: Acetone (0.05 cm^3 min^{-1}), hydrogen (50 cm^3 min^{-1}), 1 bar, 250 °C.

Conclusion

Cu-containing catalysts based on Ce-MCF and Ca-Nb-MCF supports with different copper species were prepared, characterized and applied in gas-phase acetone condensation, dehydration and hydrogenation to obtain MIBK. In the Cu/Ca-Nb-MCF catalyst was Cu^{2+} species found to interact with the silica support (Cu^{2+}-O-Si), while Cu/Ce-MCF contained both reduced Cu^0 and other Cu^{2+} forms. The different kind of copper species resulted in much more reducible forms of copper species for Cu/Ce-MCF originating from the interaction of Cu and Ce. The metal interaction promoted the catalytic performance of the Cu/Ce-MCF material significantly in the acetone transformation compared to the corresponding reference catalysts Cu/MCF and Ce-MCF, thus pointing to a synergetic interaction of the metal species. The superior performance of the Cu/Ce-MCF catalyst compared to Cu/Ca-Nb-MCF was explained by the presence of basic sites coming from ceria, necessary for the condensation of acetone to DAA, more Lewis acidity of the Cu^{2+} species required for the dehydration of DAA to MO and presence of Cu^0 centers active for the hydrogenation of MO to MIBK. Importantly, the Cu/Ce-MCF catalyst had better catalytic performance and similar durability during continuous operation for 24 h as a preferred Pd/Ce-MCF catalyst recently reported in literature,[33] implying that Cu can efficiently replace the noble metal Pd as active catalyst inventory for selective acetone condensation to MIBK.

Experimental Section

Materials. Tetraethyl orthosilicate (TEOS, >99 %) and Pluronic P123, 1,3,5-trimethylbenzene (98 %), ammonium fluoride (99.99%), ammonium niobate(V) oxalate hydrate (99.99 %), calcium acetate monohydrate (99 %), cerium(III) nitrate hexahydrate (99 %), copper(II) nitrate trihydrate (99 %) and acetone (99.5 %) were purchased from Sigma-Aldrich. Hydrochloric acid (35 wt.%) was procured from Chempur. All the chemicals were used without further purification.

Catalyst preparation. Syntheses procedures of the applied catalyst supports MCF, hydroxyapatite (HAP) and mesoporous aluminophosphate oxynitride (MAPN) are described elsewhere.[33] The latter two supports served as reference materials. The MCFs were impregnated with Ce (Ce-MCF, 20 wt.% Ce) or Nb and Ca (Ca-Nb-MCF, 20 wt.% Ca and 2 wt.% Nb) by sequential impregnation with aqueous solutions of cerium(III) nitrate hexahydrate, ammonium niobate(V) oxalate hydrate and calcium acetate monohydrate, respectively. The samples were calcined at 500 ˚C after impregnation with Nb and Ce and at 700˚C after impregnation with Ca. Cu was loaded onto the supports via wetness impregnation using aqueous solution of copper(II) nitrate trihydrate in an amount to obtain 3 wt.% loading of Cu. The catalysts were after impregnation calcined at 550 ˚C for 4 h. The prepared catalysts are denoted by the following acronyms: Cu/Ce-MCF, Cu/Ca-Nb-MCF, Cu/HAP and Cu/MAPN.

Catalyst characterization. Nitrogen physisorption was conducted on materials using a Micromeritics ASAP 2020 apparatus at -196 °C with prior outgassing of samples at 200 °C under vacuum. Surface areas were determined using the BET method, pore parameters by Broekhoff-de Boer method with BJH Fass correction (MCF), BJH method with Kruk-Jaroniec-Sayaroi correction (HAP) or DFT method with cylinder geometry (MAP, MAPN). X-ray diffraction (XRD) was performed on catalysts with a HuberG670 powder diffractometer using Cu Kα radiation (λ = 0.154 nm) within 2θ range of 20-80° in steps of 0.005°. X-ray photoelectron spectroscopy (XPS) was performed on samples as obtained and after reduction (in 50 cm^3 min^{-1} H_2 flow at 350 °C for 2 h) with an Ultra-high vacuum photoelectron spectrometer based on Phoibos 150 NAP analyzer (Specs, Germany). The analysis chamber was operated under vacuum with a pressure close to $5 \cdot 10^{-9}$ mbar and the sample was irradiated with a monochromatic Al Kα (1486.6 eV) radiation (15 kV; 10 mA). Binding energies were referenced to the Si 1s signal (103.4 eV) for Cu/Ca-Nb-MCF and Cu/Ce-MCF samples and to the C1s signal (284.6 eV) for Cu/HAP and Cu/MAPN samples. NO and pyridine adsorption combined with Fourier transform infrared (FTIR) spectroscopy was conducted on catalysts with Vertex 70 (Bruker) and Invenio (Bruker) spectrometers, respectively. Catalysts were pressed into thin wafers (5-8 mg cm^{-2}) and degassed under vacuum at 350 °C for 2 h. Then, FTIR spectra were recorded after saturation with NO gas for 30 min at room temperature, or after pyridine exposure for 5 min at 150 °C followed by outgassing under vacuum at 150, 200, 250 and 300 °C for 30 min at each temperature. The spectra of the activated samples were subtracted from the recorded spectra. Temperature programmed desorption of CO_2 (CO_2-TPD) was performed with catalysts on Micromeritics Autochem II RS232 equipment. The sample (100 mg) was heated at 550 °C in He flow (25 cm^3 min^{-1}) for 1 h. Afterwards, CO_2 adsorption was performed at 45 °C with a gas stream of CO_2 (15 cm^3 min^{-1}) diluted in He (25 cm^3 min^{-1}) for 20 min followed by flushing with He flow (25 cm^3 min^{-1}) for 1 h. Thermal desorption was then performed by heating up to 550 °C (10 °C min^{-1}) with thermal conductivity measurements every second. Temperature programmed reduction (TPR-H_2) of catalysts was also performed on a Micromeritics Autochem II RS232. The sample was heated up to 400 °C (10 °C min^{-1}) in H_2 flow (50 cm^3 min^{-1}) with thermal conductivity measurements every four second.

Catalyst testing. The prepared catalysts were examined for the reductive condensation of acetone to MIBK in gas-phase using a previously described fixed-bed reactor system.[13,33] Pelletized catalyst (100 mg, 180-355 μm) was placed in a quartz reactor and activated at 350 °C in H_2 flow (50 cm^3 min^{-1}) for 2 h, where after the reactor was cooled to 150 °C under H_2. The reaction was then performed at set-temperatures of 150, 200, 250, 300 °C, respectively, for 1 h after pumping liquid acetone (0.05 cm^3 min^{-1}) into the H_2 gas stream where it evaporated. The gaseous products were analyzed online by GC (DB-1 column, 50 m) and the components identified by standards. Catalyst stability tests were performed with selected catalysts at 250 °C for 24 h after activation as described above.

Acknowledgements

This work was supported by grant no. POWR.03.02.00-00-I026/16 co-financed by the European Union through the European Social Fund under the Operational Program Knowledge Education Development.

Keywords: acetone condensation • dehydration • hydrogenation • mesocellular foam silica • nanoparticles

[1] F. Figueras. *Top. Catal.* **2004**, *29*, 189–196.

[2] A. A. Nikolopoulos, B. W.-L. Jang, J. J. Spivey. *Appl. Catal. A Gen.* **2005**, *296*, 128–136.

[3] L. M. Gandía, R. Malm, R. Marchand, R. Conanec, Y. Laurent, M. Montes. *Appl. Catal. A Gen.* **1994**, *114*, L1–L7.

[4] D. Bomboş, G. Bozga, M. Bomboş, A. Ştefan, I. Stanciu. *Chem. Pap.* **2000**, *54*, 171–176.

[5] J. J. Gamman, S. D. Jackson, F. A. Wigzell. *Ind. Eng. Chem. Res.* **2010**, *49*, 8439–8443.

[6] C. R. Ho, S. Zheng, S. Shylesh, A. T. Bell. *J. Catal.* **2018**, *365*, 174–183.

[7] S. C. Patankar, S. K. Dodiya, G. D. Yadav. *J. Mol. Catal. A Chem.* **2015**, *409*, 171–182.

[8] N. Cheikhi, M. Kacimi, M. Rouimi, M. Ziyad, L. Liotta, G. Pantaleo, G. Deganello. *J. Catal.* **2005**, *232*, 257–267.

[9] G. Waters, O. Richter, B. Kraushaar-Czarnetzki. *Ind. Eng. Chem. Res.* **2006**, *45*, 6111–6117.

[10] R. D. Hetterley, E. F. Kozhevnikova, I. V. Kozhevnikov. *Chem. Commun.* **2006**, No. 7, 782–784.

[11] S. M. Yang, Y. M. Wu. *Appl. Catal. A Gen.* **2000**, *192*, 211–220.

[12] Y. Z. Chen, B. J. Liaw, H. R. Tan, K. L. Shen. *Appl. Catal. A Gen.* **2001**, *205*, 61–69.

[13] R. Pulikkal Thumbayil, J. Mielby, S. Kegnæs. *Top. Catal.* **2019**, *62*, 678–688.

[14] P. P. Yang, J. F. Yu, Z. L. Wang, M. P. Xu, Q. S. Liu, X. W. Yang, T. H. Wu. *Catal. Commun.* **2005**, *6*, 107–111.

[15] L. Melo, G. Giannetto, L. Cardozo, A. Llanos, L. García, P. Magnoux, M. Guisnet, F. Alvarez. *Catal. Letters* **1999**, *60*, 217–222.

[16] L. V. Mattos, F. B. Noronha, J. L. F. Monteiro. *J. Catal.* **2002**, *209*, 166–176.

[17] N. Takarroumt, M. Kacimi, F. Bozon-Verduraz, L. F. Liotta, M. Ziyad. *J. Mol. Catal. A Chem.* **2013**, *377*, 42–50.

[18] A. Alshammari, M. Mokhtar, R. Arasheed, A. Asayegh, A. Bagabas. *Top. Catal.* **2019**, *62*, 795–804.

[19] P. V. R. Rao, V. P. Kumar, G. S. Rao, K. V. R. Chary. *Catal. Sci. Technol.* **2012**, *2*, 1665.

[20] S. Narayanan, R. Unnikrishnan. *Appl. Catal. A Gen.* **1996**, *145*, 231–236.

[21] S. A. El-Molla. *Appl. Catal. A Gen.* **2006**, *298*, 103–108.

[22] G. Torres, C. R. Apesteguía, J. I. Di Cosimo. *Appl. Catal. A Gen.* **2007**, *317*, 161–170.

[23] G. Mulas, S. Deledda, G. Cocco. *Mater. Sci. Eng. A* **1999**, *267*, 214–219.

[24] T. P. S. Jadon, A. K. Jana, P. Parikh. *Biomass Conv. Bioref.* **2021**, *11*, 1093–1099.

[25] R. P. Ye, L. Lin, Q. Li, Z. Zhou, T. Wang, C. K. Russell, H. Adidharma, Z. Xu, Y. G. Yao, M. Fan. *Catal. Sci. Technol.* **2018**, *8*, 3428–3449.

[26] X. Dong, J. Lei, Y. Chen, H. Jiang, M. Zhang. *Appl. Catal. B Environ.* **2019**, *244*, 448–458.

[27] K. Chen, H. Fang, S. Wu, X. Liu, J. Zheng, S. Zhou, X. Duan, Y. Zhuang, S. Chi Edman Tsang, Y. Yuan. *Appl. Catal. B Environ.* **2019**, *251*, 119–129.

[28] M. Konsolakis. *Appl. Catal. B Environ.* **2016**, *198*, 49–66.

[29] A. Kubacka, A. Martínez-Arias, M. Fernández-García. *ChemCatChem* **2015**, *7*, 3614–3624.

[30] X. Yao, F. Gao, Q. Yu, L. Qi, C. Tang, L. Dong, Y. Chen. *Catal. Sci. Technol.* **2013**, *3*, 1355–1366.

[31] S. Sun, D. Mao, J. Yu, Z. Yang, G. Lu, Z. Ma. *Catal. Sci. Technol.* **2015**, *5*, 3166–3181.

[32] J. Zhu, Y. Su, J. Chai, V. Muravev, N. Kosinov, E. J. M. Hensen. *ACS Catal.* **2020**, *10*, 11532–11544.

[33] K. Grzelak, R. P. Thumbayil, S. Kegnæs, M. Trejda, A. Riisager. *Microporous Mesoporous Mater.* **2021**, *322*, 111169.

[34] S. T. Hossain, E. Azeeva, K. Zhang, E. T. Zell, D. T. Bernard, S. Balaz, R. Wang. *Appl. Surf. Sci.* **2018**, *455*, 132–143.

[35] A.-P. Jia, G.-S. Hu, L. Meng, Y.-L. Xie, J.-Q. Lu, M.-F. Luo. *J. Catal.* **2012**, *289*, 199–209.

[36] L. Martin, H. Martinez, D. Poinot, B. Pecquenard, F. Le Cras. *J. Phys. Chem. C* **2013**, *117*, 4421–4430.

[37] P. Gaudin, P. Fioux, S. Dorge, H. Nouali, M. Vierling, E. Fiani, M. Molière, J.-F. Brilhac, J. Patarin. *Fuel Process. Technol.* **2016**, *153*, 129–136.

[38] D. Kryszak, K. Stawicka, V. Calvino-Casilda, R. Martin-Aranda, M. Ziolek. *Appl. Catal. A Gen.* **2017**, *531*, 139–150.

[39] M. Ziolek, I. Sobczak, M. Trejda, A. Wojtaszek-Gurdak, in *Structure and Reactivity of Metals in Zeolite Materials. Structure and Bonding*, (Eds.: J. Pérez Pariente, M. Sánchez-Sánchez); Springer, Cham, **2017**; vol. 178, pp 179–249.

[40] M. C. Biesinger, L. W. M. Lau, A. R. Gerson, R. S. C. Smart. *Appl. Surf. Sci.* **2010**, *257*, 887–898.

[41] M. C. Biesinger. *Surf. Interface Anal.* **2017**, *49*, 1325–1334.

[42] I. Sobczak, M. Ziolek, M. Renn, P. Decyk, I. Nowak, M. Daturi, J.-C. Lavalley. *Microporous Mesoporous Mater.* **2004**, *74*, 23–36.

[43] M. Ziółek, I. Sobczak, I. Nowak, M. Daturi, J. C. Lavalley. *Top. Catal.* **2000**, *11/12*, 343–350.

[44] K. Kuntaiah, P. Sudarsanam, B. M. Reddy, A. Vinu. *RSC Adv.* **2013**, *3*, 7953–7962.

[45] L. Escamilla-Perea, R. Nava, B. Pawelec, M. G. Rosmaninho, C. L. Peza-Ledesma, J. L. G. Fierro. *Appl. Catal. A Gen.* **2010**, *381*, 42–53.

[46] J. M. Sánchez-Amaya, G. Blanco, F. J. Garcia-Garcia, M. Bethencourt, F. J. Botana. *Surf. Coatings Technol.* **2012**, *213*, 105–116.

[47] D. K. Dumbre, V. R. Choudhary, N. S. Patil, B. S. Uphade, S. K. Bhargava. *J. Colloid Interface Sci.* **2014**, *415*, 111–116.

[48] P. Zhu, J. Li, S. Zuo, R. Zhou. *Appl. Surf. Sci.* **2008**, *255*, 2903–2909.

[49] L. Qi, Q. Yu, Y. Dai, C. Tang, L. Liu, H. Zhang, F. Gao, L. Dong, Y. Chen. *Appl. Catal. B Environ.* **2012**, *119–120*, 308–320.

[50] S. Khabtou, T. Chevreau, J. C. Lavalley. *Microporous Mater.* **1994**, *3*, 133–148.

[51] D. He, D. Chen, H. Hao, J. Yu, J. Liu, J. Lu, F. Liu, G. Wan, S. He, Y. Luo. *Appl. Surf. Sci.* **2016**, *390*, 959–967.

[52] A. Jan, J. Shin, J. Ahn, S. Yang, K. J. Yoon, J.-W. Son, H. Kim, J.-H. Lee, H.-I. Ji. *RSC Adv.* **2019**, *9*, 27002–27012.

[53] L. Li, L. Song, C. Chen, Y. Zhang, Y. Zhan, X. Lin, Q. Zheng, H. Wang, H. Ma, L. Ding, W. Zhu. *Int. J. Hydrogen Energy* **2014**, *39*, 19570–19582.

[54] X. Zheng, X. Zhang, X. Wang, S. Wang, S. Wu. *Appl. Catal. A Gen.* **2005**, *295*, 142–149.

10.1002/cssc.202102012

Entry for the Table of Contents

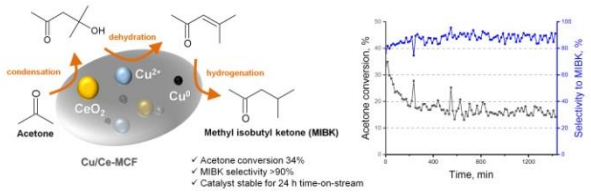

Copper is demonstrated as an efficient and cheap substitute for palladium in mesocellular foam silica catalyst applied for the production of methyl isobutyl ketone, which is an important solvent in the industry.